Three-Leg Active Bridge-Based Bidirectional Resonant Converter Using Hybrid Si/SiC Switches

Cheol-Hwan Kim, *Student Member, IEEE*, Changkyu Bai, *Member, IEEE*, Sang-Won Lee, *Member, IEEE*, Eun-Ha Park, and Minsung Kim, *Senior Member, IEEE*

***Abstract*—This article proposes a bidirectional resonant converter that uses a three-leg active bridge and hybrid Si/SiC switches. The use of a three-leg active bridge on the secondary side of the transformer transfers twice as much power compared with the use of a single active bridge; one of the three legs is shared, which reduces the number of active power devices in the development process. The phase-shift modulation has been adopted for both power flow directions, which enables zero-voltage switching turn-ON for all the switches. On the secondary side, the shared leg only requires the use of two SiC MOSFETs, because these particular switches undergo high conduction loss and high turn-OFF loss during both forward and backward operations. This trait reduces the implementation cost of the circuit further. The primary-side windings of the transformer are connected in series and each secondary-side winding has wound in the opposite direction. The resulting symmetric architecture of the dual transformer connected to a three-leg active bridge and the corresponding pulsewidth modulation (PWM) naturally balance the currents flowing through the middle leg and right leg on the secondary side. A 1-kW rated prototype that converts 150–200 V input to a 400 V output is designed and tested to validate the concept for cost-effective battery charging and discharging.**

***Index Terms*—DC-DC power converters, power conversion, power semiconductor devices, resonant converters.**

I. Introduction

BATTERIES are an efficient source of energy and one of the most convenient mediums to store power. Electric automobiles, such as electric cars, electric scooters, and aerial electric vehicles, have an increasing demand for battery-powered machinery and equipment. Also, the intermittent nature of renewable energy sources, such as solar panels, thermoelectric modules, and small-size wind turbines, necessitates the use of batteries. Of course, the primary driving force behind the growth of the global battery market is the significant expansion of the electric automobile industry. It is projected that the global battery industry will achieve a worth of $182.96 billion by 2027, with a compound annual growth rate of 9.20% during the period spanning from 2022 to 2027 [1]. The battery voltage can vary from very low to high when it is charged from a deeply discharged state. Besides, the power capacity of recently developed batteries is increasing. Therefore, the converters that interface between a dc bus and a battery must be highly efficient, tolerate high power, and be able to operate under a wide range of battery voltage.

Single-phase linear-type bidirectional topologies have been widely evaluated for bidirectional power transfer applications. Different topologies, such as bidirectional flyback [2], [3], push–pull [4], [5], [6], dual half-bridge [7], [8], dual active bridge (DAB) [9], [10], [11], [12], and other topologies have been selected for bidirectional dc/dc converter. DAB converters have become preferred because they benefit from high power density and straightforward control logic. By means of two active bridges and the phase shift between them, a DAB converter can accomplish simple bidirectional power conversion. Nevertheless, the switches may experience high current when turned OFF, they cannot guarantee zero-voltage switching (ZVS) turn-ON over a wide spectrum of battery voltage.

A series resonant converter usually consists of a full bridge or a half bridge at the primary side, a resonant tank at the secondary side, and a diode bridge at the secondary side; the switching modulation is applied to the full bridge or the half bridge at the primary side. Then, this converter can transfer the power with soft switching, but it is inherently buck-type. If the buck operation is necessary for power to flow in one direction, then the boost operation will naturally be needed for power to flow in the opposite direction. However, the operation of this buck-type converter is valid only in the forward power flow direction. To enable bidirectional power transfer for the resonant converter, a *CLLC* resonant tank has been adopted in the converters in [13], [14], and [15]. These converters can accomplish soft switching by using primary-side and secondary-side series resonant tanks. To ensure uniform characteristics for

Manuscript received 30 December 2023; revised 28 March 2024; accepted 23 April 2024. Date of publication 6 May 2024; date of current version 20 June 2024. This work was supported in part by the National Research Foundation of Korea (NRF), Korea government (MSIT), under Grant RS-2023-00210590, in part by the National Research Foundation of Korea (NRF), Korea government (MSIT), under Grant RS-2023-00269940, in part by the Korea Basic Science Institute (National research Facilities and Equipment Center) Ministry of Education under Grant 2020R1A6C101A187, and in part by the Human Resources Development Project of the Korea Institute of Energy Technology Evaluation and Planning (KETEP), Korea government Ministry of Trade, Industry, and Energy through the project titled: "Middle market enterprise specialized human resources development for residential and commercial fuel cell," under Grant 20224000000580. Recommended for publication by Associate Editor Xiaoze Pei. *(Corresponding author: Minsung Kim.)*

Cheol-Hwan Kim, Eun-Ha Park, and Minsung Kim are with the Division of Electronics and Electrical Engineering, Dongguk University, Jung-gu, Seoul 04620, South Korea (e-mail: regin1006@dgu.ac.kr; christin13@dgu.ac.kr; mkim@dgu.ac.kr).

Changkyu Bai is with the Global Research and Development Center, Mando, Seongnam 13486, South Korea (e-mail: changkyu.bai@hlcompany.com).

Sang-Won Lee is with the Department of Electrical, Electronics and Control Engineering, Kongju National University, Cheonan 31080, South Korea (e-mail: swlee@kongju.ac.kr).

Color versions of one or more figures in this article are available at https://doi.org/10.1109/TPEL.2024.3396848.

Digital Object Identifier 10.1109/TPEL.2024.3396848

bidirectional power transfer, the secondary *LC* resonant tank is designed to be the same as the primary *LC* resonant tank. However, when battery voltage varies widely, the symmetric *CLLC* design can lead to the operation at an undesirable high switching frequency. To address this problem, an asymmetric *CLLC* resonant tank design has been proposed in [16] and [17], but the design of a resonant tank becomes complicated. Furthermore, the hard switching problem can still occur when battery voltage varies widely. Resonant DAB converters [18], [19], [20], [21] are capable of achieving soft switching while preserving the buck/boost capability of the DAB converter. However, when the battery voltage varies widely, the converter experiences high instantaneous reactive current, which causes an increase in conduction loss, thus reducing the efficiency of power conversion. A resonant DAB converter in [22] has reduced instantaneous reactive current at higher output power. However, it still suffers from high instantaneous reactive current when the battery voltage varies widely. A bidirectional resonant converter using a T-type active voltage doubler has been proposed to address this problem [23]. In the forward power flow, this converter operates as a full-bridge resonant boost converter by switching the high-voltage side switches at a high frequency. When power flows in the opposite direction, it is activated as a T-type resonant buck converter. The switches achieve soft switching by utilizing the voltage fluctuation of the resonant capacitor. Nonetheless, when operating at higher power levels, the current flowing through the active power components on the high-voltage side increases. This causes MOSFETs that have high voltage ratings to experience high conduction loss, leading to heat accumulation. The interleaving structure [24] can help distribute the heat among the switches, but this structure also significantly increases the number of power components.

To overcome this problem, we propose a bidirectional resonant dc/dc converter that uses a three-leg active bridge, with the goal of obtaining high power transfer. Main contributions can be summarized as follows.

1) By incorporating the three-leg active bridge on the secondary-side of the transformer, we can transfer the same power as the converter with two full-bridge circuits on the secondary side; the left leg is shared in the power processing and so reduces the development cost.
2) The conventional duty modulation can turn on the switches at the secondary-side left leg with ZCS. In contrast, the proposed phase-shift modulation enables all the switches turned ON with ZVS for both power flow directions.
3) The conventional duty modulation can generate high turn-OFF switching loss at the secondary-side four switches in both power flow directions. On the contrary, the proposed phase-shift modulation generates high turn-OFF switching loss only at the secondary-side left leg in both power flow directions; the use of SiC MOSFETs only on that leg further reduces development cost.
4) This symmetric configuration of the transformer with regard to the middle point of the secondary side winding balances the current flowing through the secondary-side middle leg and right leg. To confirm the proposed analysis and design, a 1-kW prototype was constructed.

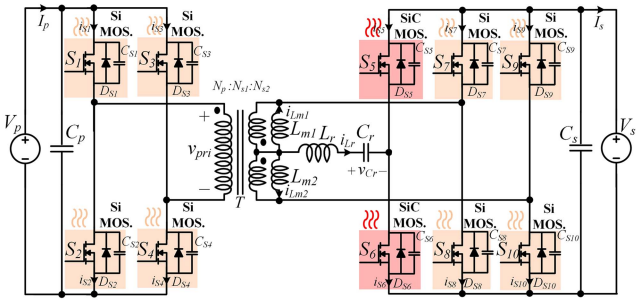

Fig. 1. Schematic diagram of the proposed bidirectional converter; the hard-switching and soft-switching parts are highlighted in red and orange backgrounds, respectively.

The rest of this article is organized as follows. Section II describes how the bidirectional resonant converter operates, while Section III examines its steady-state performance. Section IV provides an in-depth analysis of the design considerations. The experimental results are presented in Section V. Discussion is shown in Section VI. Finally, Section VII concludes this article.

II. Topology Description and Operating Principles

The proposed bidirectional converter (see Fig. 1) comprises a full-bridge circuit, a dual transformer, and three active-leg bridges. In Fig. 1, the circuit components are labeled as follows: switches are denoted by S_i, $D_{S'i'}$, and $C_{S'i'}$ (i ranging from 1 to 10); the transformer is represented by T and has a turns ratio of $n = (N_{s1} + N_{s2})/N_p$ and N_p:N_{s1}:N_{s2}, where N_p is the number of primary winding turns, N_{s1} is the number of upper-side primary winding turns, and N_{s2} is the number of lower-side secondary winding turns. Other circuit components and electrical quantities are the upper-side secondary magnetizing inductor (L_{m1}), lower-side secondary magnetizing inductor (L_{m2}), resonant inductor (L_r), resonant capacitor (C_r), primary capacitor (C_p), secondary capacitor (C_s), a primary voltage source (V_p), a secondary voltage source (V_s), the voltage across C_r (v_{Cr}), primary voltage of T (v_{pri}), upper secondary magnetizing current (i_{Lm1}), lower secondary magnetizing current (i_{Lm2}), current through L_r (i_{Lr}), current through S_i ($i_{S'i'}$), primary current (I_p), and secondary current (I_s).

During forward operation, the converter operates as a pulsewidth modulation (PWM) resonant boost converter, where S_1 and S_4 form one diagonal switch pair, and S_2 and S_3 form the other. Two pairs of diagonal switches are controlled by two PWM signals that have the same duty cycle of $0.5-t_{df}/T_s$ and the same dead-time t_{df}, but are out of phase with each other by 180°. S_5 is turned ON immediately after S_2 and S_3, and turned OFF in D_fT_s. S_6 is turned ON immediately after S_1 and S_4, and turned OFF in D_bT_s. S_7–S_{10} are always OFF. The variable duty modulation in forward operation results in zero-current-switching (ZCS) turns ON at S_5 and S_6 (see Table I). By adopting the variable phase-shift modulation in forward operation, S_5 and S_6 can be turned ON with ZVS. Also, this modulation can reduce the conduction loss because the current flows while these switches are turned ON. In this variable phase-shift modulation, S_5 and S_6 are controlled by two same PWM signals used for

TABLE I
HARD-SWITCHING/SOFT-SWITCHING COMPONENTS ACCORDING TO THE SWITCHING MODULATION

No.	Modulation	Turn-OFF with hard-switching	Turn-ON/OFF with soft-switching
1	Variable duty modulation in forward operation	S_5,S_6	S_1–S_4
2	Variable phase-shift modulation in forward operation	S_5,S_6	S_1–S_4
3	Variable duty modulation in backward operation	S_5,S_7,S_9	S_6,S_8,S_{10}
4	Variable phase-shift modulation in backward operation	S_5,S_6	S_7–S_{10}

*In case 1, S_5 and S_6 are turned ON with ZCS.

*In case 2, S_5 and S_6 are turned ON with ZVS.

(S_1, S_4) and (S_2, S_3), but adjusted with $2\pi D_f/T_s$ degrees of phase. During backward operation, the converter operates as a PWM resonant buck converter, where S_5, S_7, and S_9 form one switch group, and S_6, S_8, and S_{10} form another switch group. Both groups are driven by two PWM signals that have the same duty cycle of $0.5-t_{db}/T_s$ and the same dead-time t_{db}, but are out of phase with each other by $2\pi D_b/T_s$ degrees. S_1–S_4 are always OFF. The use of variable duty modulation in backward operation results in turn-OFF with hard-switching at S_5, S_7, and S_9 [25], but the variable phase-shift modulation in backward operation results in turn-OFF with hard-switching at S_5 and S_6 as in forward operation (see Table I). By adopting the variable phase-shift modulation, only two SiC switches are needed for S_5 and S_6. In this variable phase-shift modulation, (S_7, S_9) and (S_8, S_{10}) are controlled by two same PWM signals used for S_6 and S_5, but adjusted with $2\pi D_b/T_s$ degrees of phase.

We make the following two assumptions to formulate the circuit equations that correspond to different operating states in the steady-state.

1) The switches S_1 through S_{10} are ideal, except for their body diodes (D_{S1} to D_{S10}) and output capacitors (C_{S1} to C_{S10}). The capacitance values for C_{S1} through C_{S4} are equal, C_{S5} is equal to C_{S6}, and C_{S7} through C_{S10} are equal.
2) The transformer is characterized by magnetizing inductance L_{m1} and L_{m2} as well as secondary leakage inductance. The leakage inductance of the transformer is connected in series with an external inductance to make up L_r. Both L_{m1} and L_{m2} have the same values.

In the steady-state analysis, the proposed converter is split into four states in forward and backward operations during the half switching period $T_s/2$. The description of states is only given for the first-half switching period due to the symmetric operation. (Figs. 2–5).

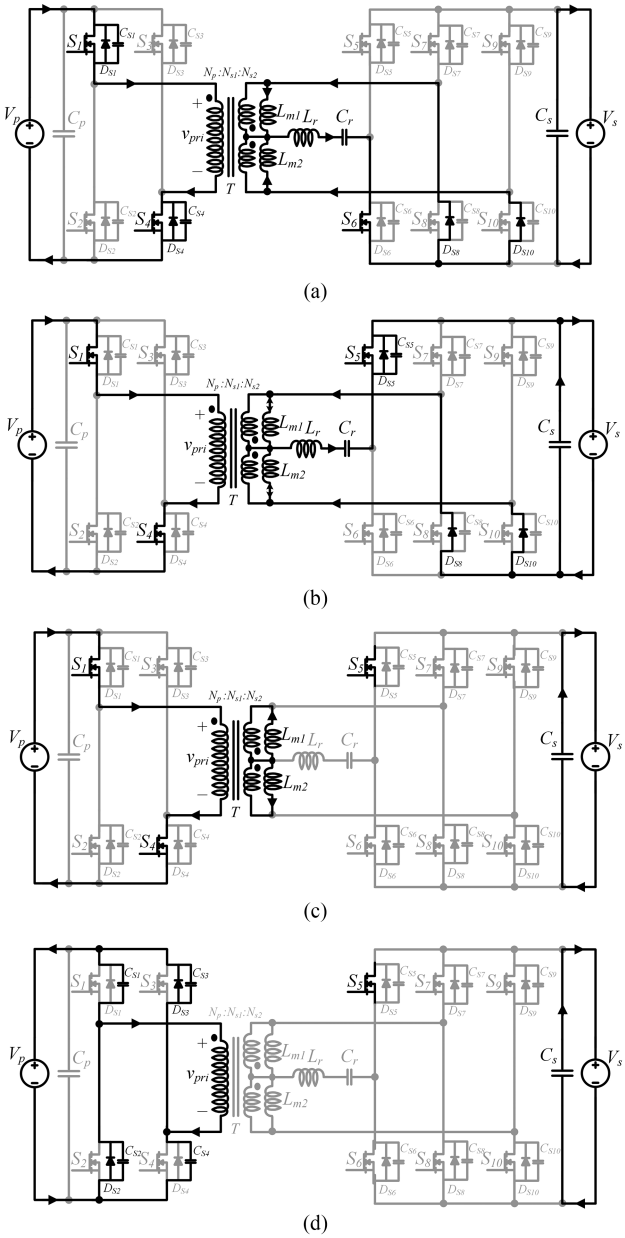

Fig. 2. Equivalent circuits during the first half of the switching period in forward operation. (a) State 1. (b) State 2. (c) State 3. (d) State 4.

A. Analysis in Forward Operation

State 1 [t_0, t_1]: At time t_0, S_1 and S_4 are turned ON with ZVS as their corresponding diodes D_{S1} and D_{S4} are already conducting. D_{S8} and D_{S10} are acting as diodes [see Fig. 2(a)]. i_{Lr} resonates with v_{Cr}; i_{Lr} increases quickly (see Fig. 3). The state equation is formulated as

$$L_r\frac{di_{Lr}(t)}{dt} = 0.5nV_p + v_{Cr}(t), \quad i_{Lr}(t) = C_r\frac{dv_{Cr}(t)}{dt} \tag{1}$$

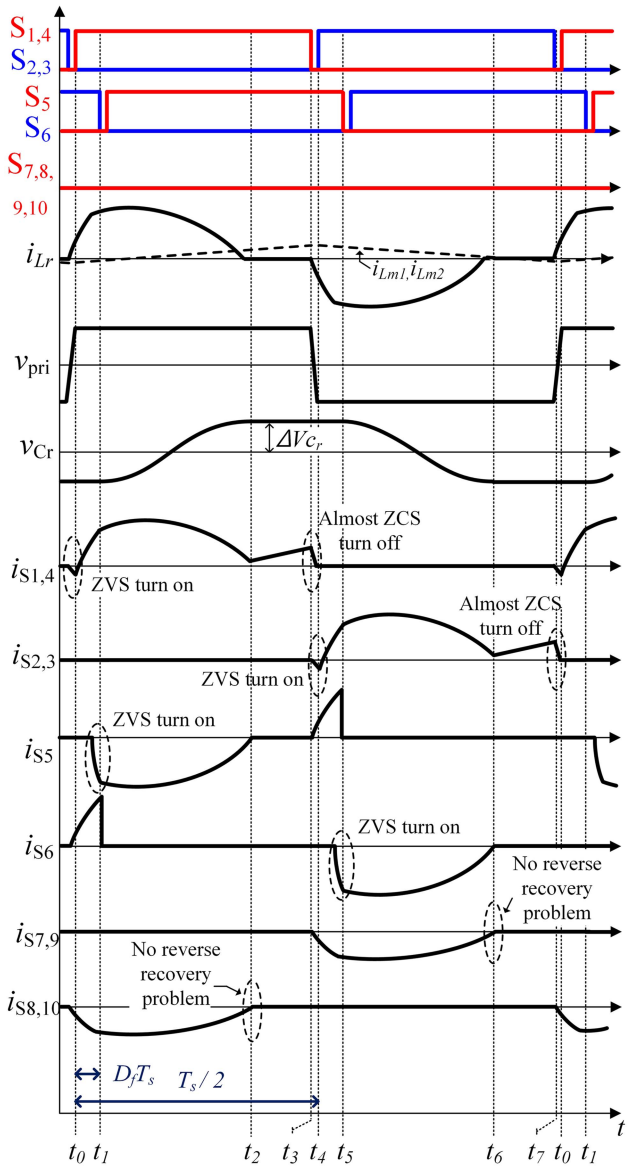

Fig. 3. Theoretical waveforms in forward operation. $S_{i'}$ is the gate-source voltage of the 'i''th switch.

with $i_{Lr}(t_0) = 0$ and $v_{Cr}(t_0) = 0.5nV_p - r_1 \cos\pi$. Solving (1)

$$i_{Lr}(t) = \frac{r_1}{Z_r}\sin(\pi - \omega_r(t - t_0)) \tag{2}$$

$$v_{Cr}(t) = 0.5nV_p + r_1\cos(\pi - \omega_r(t - t_0)) \tag{3}$$

with the radius of the trajectory path $r_1 = 0.5nV_p + \Delta V_{cr}$, the resonant angular frequency $\omega_r = \frac{1}{\sqrt{L_r C_r}}$, and the characteristic impedance $Z_r = \sqrt{\frac{L_r}{C_r}}$ where ΔV_{cr} is the voltage ripple of the resonant capacitor.

State 2 [t_1, t_2]: At time t_1, S_6 is turned OFF. S_5 is turned ON with ZVS as its corresponding diode D_{S5} is already conducting. D_{S6}, D_{S8}, and D_{S10} are acting as diodes [see Fig. 2(b)]. In this interval, i_{Lr} resonates with v_{Cr} (see Fig. 3), but with different applied voltages; i_{Lr} goes to zero sinusoidally. The state equation is presented as

$$L_r\frac{di_{Lr}(t)}{dt} = 0.5nV_p - V_s + v_{Cr}(t),\;\; i_{Lr}(t) = C_r\frac{dv_{Cr}(t)}{dt} \tag{4}$$

with $i_{Lr}(t_1) = \frac{r_2}{Z_r}\sin\alpha$ and $v_{Cr}(t_1) = 0.5nV_p - V_s + r_2\cos\alpha$, where $\alpha = \cos^{-1}(\frac{r_1}{r_2}\cos(\pi - \omega_r(t_1 - t_0)) + \frac{V_s}{r_2})$. Solving (4)

$$i_{Lr}(t) = \frac{r_2}{Z_r}\sin(\alpha - \omega_r(t - t_1)) \tag{5}$$

$$v_{Cr}(t) = 0.5nV_p - V_s + r_2\cos(\alpha - \omega_r(t - t_1)) \tag{6}$$

with the radius of the trajectory path $r_2 = -0.5nV_p + V_s + \Delta V_{cr}$.

State 3 [t_2, t_3]: At time t_2, i_{Lr} becomes zero and v_{Cr} reaches at its maximum. In this interval, ni_{Lm1}, ni_{Lm2} flow through S_1 and S_4 [see Fig. 2(c)]; the value of i_{Lm} is kept small since L_m is typically selected with a large value. Consequently, (S_1, S_4) is turned OFF with almost ZCS at time t_3 (see Fig. 3).

State 4 [t_3, t_4]: At time t_3, S_1 and S_4 are turned OFF with almost ZCS. In this interval, ni_{Lm1} and ni_{Lm2} appear as a current source to the primary side, charging C_{S1} and C_{S4} and discharging C_{S2} and C_{S3} [see Fig. 2(d)]. This causes S_2 and S_3 to turn ON with ZVS in the subsequent state [see Fig. 3]. During the second half switching period, the waveforms in states 1, 2, 3, and 4 are symmetrical to those of the first half.

B. Analysis in Backward Operation

State 1 [t_0, t_1]: At time t_0, the voltages across S_7 and S_9 are zero and i_{Lr} flows through D_{S7} and D_{S9}, with S_7 and S_9 turned ON using ZVS. D_{S2} and D_{S3} are acting as diodes [see Fig. 4(a)]. i_{Lr} resonates with v_{Cr}; i_{Lr} increases sinusoidally (see Fig. 5). In this interval, the state equation is formulated as

$$L_r\frac{di_{Lr}(t)}{dt} = 0.5nV_p - V_s + v_{Cr}(t),\;\; i_{Lr}(t) = C_r\frac{dv_{Cr}(t)}{dt} \tag{7}$$

with $i_{Lr}(t_0) = 0$ and $v_{Cr}(t_0) = 0.5nV_p - V_s + r_3$. Solving (7)

$$i_{Lr}(t) = \frac{r_3}{Z_r}\sin(\omega_r(t - t_0)) \tag{8}$$

$$v_{Cr}(t) = 0.5nV_p - V_s + r_3\cos(\omega_r(t - t_0)) \tag{9}$$

with the radius of the trajectory path $r_3 = -0.5nV_p + V_s + \Delta V_{cr}$.

State 2 [t_1, t_2]: At time t_1, S_6 is turned OFF. After the dead time, S_5 is then turned ON with ZVS as its corresponding diode D_{S5} is conducting. D_{S2} and D_{S3} are still acting as diodes [see Fig. 4(b)]. In this interval, i_{Lr} resonates with v_{Cr}, but with different applied voltages; i_{Lr} goes to zero quickly (see Fig. 5). The state equation is

$$L_r\frac{di_{Lr}(t)}{dt} = 0.5nV_p + v_{Cr}(t),\;\; i_{Lr}(t) = C_r\frac{dv_{Cr}(t)}{dt} \tag{10}$$

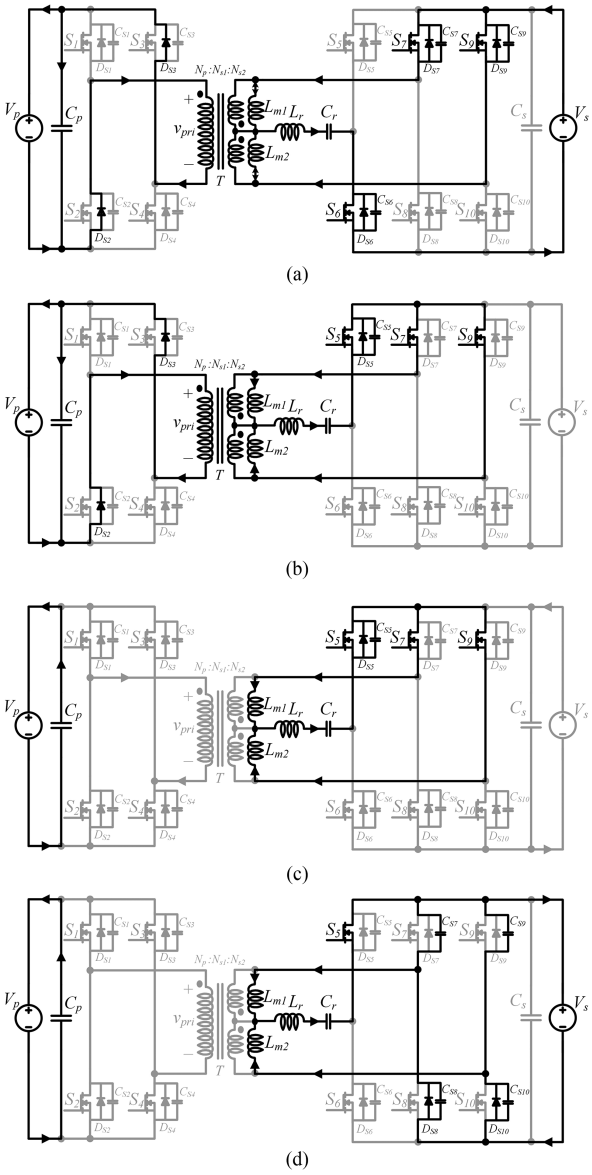

Fig. 4. Equivalent circuits during the first half of the switching period in backward operation. (a) State 1. (b) State 2. (c) State 3. (d) State 4.

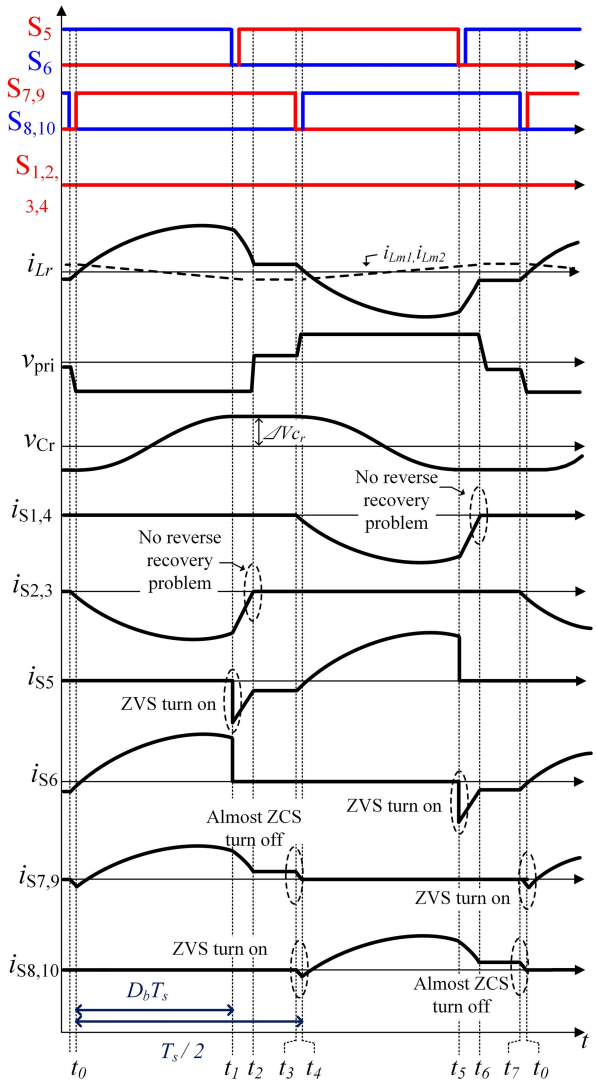

Fig. 5. Theoretical waveforms in backward operation.

with $i_{Lr}(t_1) = \frac{r_4}{Z_r}\sin\beta$ and $v_{Cr}(t_1) = 0.5nV_p + r_4\cos\beta$, where $\beta = \cos^{-1}(\frac{r_3}{r_4}\cos(\omega_r(t_1 - t_0)) + \frac{V_s}{r_4})$. Solving (10)

$$i_{Lr}(t) = \frac{r_4}{Z_r}\sin(\beta - \omega_r(t - t_1)) \tag{11}$$

$$v_{Cr}(t) = 0.5nV_p + r_4\cos(\beta - \omega_r(t - t_1)) \tag{12}$$

with the radius of the trajectory path $r_4 = 0.5nV_p + \Delta V_{cr}$.

State 3 [t_2, t_3]: At time t_2, The magnetizing current flows through S_7 and S_9 [see Fig. 4(c)]. By selecting L_{m1} and L_{m2} to make i_{S7} and i_{S9} very small, S_7 and S_9 can be turned OFF with almost ZCS (see Fig. 5).

State 4 [t_3, t_4]: At time t_3, S_7 and S_9 are turned OFF with almost ZCS, and the converter enters the dead-time zone. The current ni_{Lm1} and ni_{Lm2} act as a current source to the low-voltage side, charging C_{S7} and C_{S9} and discharging C_{S8} and C_{S10} [see Fig. 4(d)]. When C_{S8} and C_{S10} are fully discharged, i_{Lm1} and i_{Lm2} flow through D_{S8} and D_{S10}, and S_8 and S_{10} are turned ON with ZVS (see Fig. 5).

III. Steady-State Analysis

A. Voltage Conversion Ratio in Forward Operation

To determine the voltage conversion ratio of the proposed converter in the forward operation, the first step is to compute ΔV_{Cr}. The resonant current during the switching period is equivalent to the average output current, and it can be calculated as

$$I_s = \frac{P_s}{V_s} = \frac{1}{T_s}\left[\int_{t_0}^{t_1}\frac{r_1}{Z_r}\sin[\pi - \omega_r(\tau - t_1)]d\tau + \int_{t_1}^{t_2}\frac{r_2}{Z_r}\sin[\alpha - \omega_r(\tau - t_2)]d\tau\right] = \frac{2nV_pC_r\Delta V_{Cr}}{T_sV_s}. \tag{13}$$

Rearranging (13) for ΔV_{Cr} yields

$$\Delta V_{Cr} = \frac{P_s T_s}{2nV_p C_r}. \tag{14}$$

From (2)–(6), we have the circle equations for states 1 and 2

$$(v_{Cr}(t) - 0.5nV_p)^2 + (Z_r i_{Lr}(t))^2 = r_1^2 \tag{15}$$

$$(v_{Cr}(t) - 0.5nV_p - V_s)^2 + (Z_r i_{Lr}(t))^2 = r_2^2. \tag{16}$$

The two circles meet at $t = t_1$, so equating (15) and (16) at $t = t_1$ yields

$$(v_{Cr}(t_1) - 0.5nV_p)^2 - r_1^2 = (v_{Cr}(t_1) - 0.5nV_p + V_s)^2 - r_2^2. \tag{17}$$

Applying $(t_1 - t_0) = D_f T_s$ and (14) to (17), we have

$$D_f = \frac{1}{\omega_r T_s} \cos^{-1}\left(\frac{V_s P_s T_s M_f (2 - M_f) + 4V_s^3 C_r}{4V_s^3 C_r + V_s P_s T_s M_f^2}\right) \tag{18}$$

where $M_f = \frac{2V_s}{nV_p}$ is the voltage conversion ratio of the proposed converter operating in forward operation.

Rearranging (18) for M_f gives

$$M_f = \frac{B_f + \sqrt{B_f^2 - 4B_f C_f (A_f^2 - 1)}}{B_f (A_f + 1)} \tag{19}$$

with $A_f = \cos(\omega_r T_s D_f)$, $B_f = V_s P_s T_s$, and $C_f = V_s^3 C_r$.

Fig. 6(a) shows a 3-D plot of M_f as a function of D_f and P_s.

B. Voltage Conversion Ratio in Backward Operation

By applying the identical approach used to obtain the voltage conversion ratio in the forward operation, we have

$$I_s = \frac{P_s}{V_s} = \frac{1}{T_s}\left[\int_{t_0}^{t_1} \frac{r_3}{Z_r} \sin[\omega_r(\tau - t_1)] d\tau + \int_{t_1}^{t_2} \frac{r_4}{Z_r} \sin[\alpha - \omega_r(\tau - t_2)] d\tau\right] = \frac{4C_r \Delta V_{Cr}}{T_s}. \tag{20}$$

Rearranging (13) for ΔV_{Cr} yields

$$\Delta V_{Cr} = \frac{P_s T_s}{4V_s C_r}. \tag{21}$$

From (8)–(12), we have the circle equations for states 1 and 2

$$(v_{Cr}(t) - 0.5nV_p + V_s)^2 + (Z_r i_{Lr}(t))^2 = r_3^2 \tag{22}$$

$$(v_{Cr}(t) - 0.5nV_p)^2 + (Z_r i_{Lr}(t))^2 = r_4^2. \tag{23}$$

The two circles meet at $t = t_1$, so equating (22) and (23) at $t = t_1$ yields

$$(v_{Cr}(t_1) - 0.5nV_p + V_s)^2 - r_3^2 = (v_{Cr}(t_1) - 0.5nV_p)^2 - r_4^2. \tag{24}$$

Applying $(t_1 - t_0) = D_b T_s$ and (21) to (24) yields

$$D_b = \frac{1}{\omega_r T_s} \cos^{-1}\left(\frac{V_s P_s T_s (2M_b - 1) + 4V_s^3 C_r (M_b - 1)}{4V_s^3 C_r (M_b - 1) - V_s P_s T_s}\right) \tag{25}$$

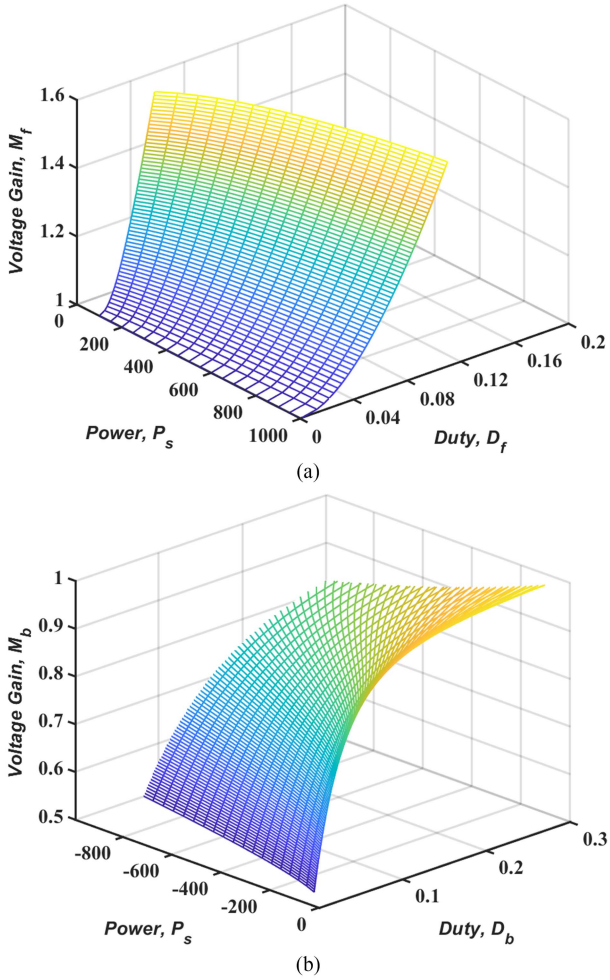

Fig. 6. 3-D plots of voltage conversion ratios of proposed converter as a function of duty cycle and power. (a) M_f. (b) M_b.

where $M_b = \frac{nV_p}{2V_s}$ is the voltage conversion ratio of the proposed converter operating in backward operation.

Rearranging (25) for M_b gives

$$M_b = \frac{A_b B_b + A_b C_b - B_b - C_b}{A_b B_b - B_b - 2C_b} \tag{26}$$

where $A_b = \cos(\omega_r T_s D_b)$, $B_b = 4V_s^3 C_r$, and $C_b = V_s P_s T_s$.

Fig. 6(b) shows a 3-D plot of M_b as a function of D_b and P_s.

IV. Design Consideration

A. Turns Ratio of Transformer

The voltage conversion ratio of the proposed bidirectional converter can be used to find the turns ratio of the transformer. The maximum possible value for the turns ratio n is calculated by dividing twice the secondary source voltage V_s by maximum primary source voltage V_{p_max}.

$$n \le \frac{2V_s}{V_{p\_max}} = \frac{2 \times 400}{200} = 4.00. \tag{27}$$

According to (27), the resulting n becomes 4.0.

B. Magnetics Design

To set the size of the cores for the transformer and resonant external inductor, we need to obtain core geometry K_g first [27]. The magnetics design was conducted when the peak current flows through the circuit within the predetermined input/output voltage range and at full load. The peak current flowing through the upper magnetizing inductor $i_{pk,Lm1}$ is 2.8 A; the total current flowing through primary-side winding and secondary-side winding of the upper transformer $i_{\text{tot},Tr1} = i_{\text{pri}} + n \times i_{\text{sec1}}$ is 19.2 A; the peak current flowing through resonant inductor $i_{pk.Lr}$ is 15.5 A; root mean square current flowing through external resonant inductor $i_{\text{rms},Lr}$ is 6.4 A; we set the peak of magnetic flux density for the upper transformer $B_{pk,Tr1}$ as 0.17 and for the resonant external inductor $B_{pk,Lr}$ as 0.16 to ensure low transformer core loss; the copper losses at the upper transformer and the resonant external inductor are assumed to be $P_{cu,\text{loss},Tr1}$=11.3 W and $P_{cu,\text{loss},Lr}$=3.68 W; we set window utilization constant for the upper transformer $K_{u,Tr1}$ as 0.5 and we set window utilization constant for the resonant external inductor $K_{u,Lr}$ as 0.4. Then, we have the following core geometry for the upper transformer and the resonant external inductor:

$$K_{g,Tr1} \geq \frac{\rho L_{m1}^2 i_{pk,Lm1}^2 i_{\text{tot},Tr1}^2}{B_{pk,Tr1}^2 P_{cu,\text{loss},Tr1} K_{u,Tr1}} \times 10^8 = \frac{1.7 \times 10^{-6} \times (700 \times 10^{-6})^2 \times 2.8^2 \times 19.2^2}{0.17^2 \times 11.3 \times 0.5} \times 10^8 = 1.474 \text{ cm}^5 \quad (28)$$

$$K_{g,Lr} \geq \frac{\rho L_r^2 i_{pk,Lr}^2 i_{rms,Lr}^2}{B_{pk,Lr}^2 P_{cu,loss,Lr} K_{u,Lr}} \times 10^8 = \frac{1.7 \times 10^{-6} \times (30 \times 10^{-6})^2 \times 15.5^2 \times 6.4^2}{0.16^2 \times 3.68 \times 0.4} \times 10^8 = 0.039 \text{ cm}^5 \quad (29)$$

where ρ = resistivity = $1.7 \times 10^{-6} \Omega$·cm. According to [28] and considering core geometry for transformer and resonant external inductor, we used PQ5050 for transformer core and PQ3535 for resonant external inductor core.

Second, we set the airgap according to the following equations:

$$L_{g,Tr1} \geq \frac{\mu_0 L_{m1} i_{pk,Lm1}^2}{B_{pk,Tr1}^2 A_{c,PQ5050}} \times 10^4 = \frac{4\pi \times 10^{-7} \times 700 \times 10^{-6} \times 2.8^2}{0.17^2 \times 3.28} \times 10^4 = 0.727 \text{ mm} \quad (30)$$

$$L_{g,Lr} \geq \frac{\mu_0 L_r i_{pk,Lr}^2}{B_{pk,Lr}^2 A_{c,PQ3535}} \times 10^4 = \frac{4\pi \times 10^{-7} \times 30 \times 10^{-6} \times 15.5^2}{0.16^2 \times 1.96} \times 10^4 = 1.805 \text{ mm} \quad (31)$$

where μ_0 = permeability of free space $= 4\pi \times 10^{-7}$ H/m, $A_{c,PQ5050} = 3.28$ cm^2, and $A_{c,PQ3535} = 1.96$ cm^2.

Third, we set the number of turns according to the following equations:

$$N_{s1} \geq \frac{L_{m1} i_{pk,Lm1}}{B_{pk,Tr1} A_{c,PQ5050}} \times 10^4 = \frac{700 \times 10^{-6} \times 2.8}{0.17 \times 3.28} \times 10^4 = 35.15 \quad (32)$$

$$N_{Lr} \geq \frac{L_r i_{pk,Lr}}{B_{pk,Lr} A_{c,PQ3535}} \times 10^4 = \frac{30 \times 10^{-6} \times 15.5}{0.16 \times 1.96} \times 10^4 = 14.82. \quad (33)$$

According to (32), we set the number of turns for the secondary-side of the upper and lower transformers as $N_{s1} = N_{s2} = 36$. Then, the number of turns for the primary-side of the transformer is obtained as $N_p = \frac{N_{s1}+N_{s2}}{n} = 18$. According to (33), we set the number of turns for the resonant external inductor as 19.

Finally, we obtain the allocation of window area as

$$\alpha_p = \frac{i_{\text{pri}}}{i_{\text{tot},Tr1}} = 0.34 \quad (34)$$

$$\alpha_{s1} = \frac{n i_{\text{sec1}}}{i_{\text{tot},Tr1}} = 0.66. \quad (35)$$

Window area from the core PQ5050 is obtained as $W_{a,PQ5050} = 4.33$ cm^2; window area from the core PQ3535 is obtained as $W_{a,PQ3535} = 2.20$ cm^2. Then, we obtain the wire area as

$$A_{W,p} \leq \frac{\alpha_p K_{u,Tr1} W_{a,PQ5050}}{N_p} = 0.0408 \text{ cm}^2 \quad (36)$$

$$A_{W,s1} \leq \frac{\alpha_s K_{u,Tr1} W_{a,PQ5050}}{N_{s1}} = 0.0384 \text{ cm}^2 \quad (37)$$

$$A_{W,Lr} \leq \frac{K_{u,Lr} W_{a,PQ3535}}{N_{Lr}} = 0.0488 \text{ cm}^2. \quad (38)$$

At the switching frequency of 100 kHz, the recommended diameter of single strand of litz wire is 38 AWG. To satisfy (36)–(38), we set the number of strands for the primary-side winding of the transformer, the secondary-side winding of the transformer, and the winding of the resonant external inductor as 340, 260, and 200.

C. Magnetizing Inductance

Compared with the switching period, the dead times of the primary-side switches in forward operation (t_{df}) and the secondary-side switches in backward operation (t_{db}) are very short. Then, i_{Lm1} and i_{Lm2} act as constant current sources I_{Lm1} and I_{Lm2}. If the magnitude of i_{Lm1} is very high, we can only consider I_{Lm1} in obtaining the ZVS region. However, the magnitude of i_{Lm1} is not very high in the proposed converter. To obtain the ZVS region accurately in forward operation, we need to consider both i_{Lm1} and i_{Lr}. During the dead time in the forward operation, i_{Lm1} and i_{Lr} discharge C_{S2} and C_{S3} and charges C_{S1} and C_{S4}. To attain ZVS, i_{Lm} should fully discharge C_{S2}, C_{S3}. Thus, the ZVS condition in the forward operation is obtained and simplified using $\sin(\omega_r t) \simeq \omega_r t$ when $\omega_r t$ is very

small

$$V_p C_{s2} < \left| \int_0^{t_{df}} \left[n \cdot (i_{Lm1}(\tau) + i_{Lr}(\tau)) \right] d\tau \right| \simeq n I_{Lm1} t_{df} - \frac{r_1 \omega_r t_{df}^2}{2 Z_r} (\omega_r \tau). \quad (39)$$

Substituting $I_{Lm1} = \frac{nV_p T_s}{8L_{m1}}$ into (39) yields

$$L_{m1} < \frac{n^2 V_p T_s t_{df}}{8 V_p C_{S2} + 4 r_1 \omega_r t_{df}^2 / Z_r} \simeq \begin{cases} 1,500\,\mu\text{H} & \text{when } P_s = 1\,\text{kW} \\ 2,200\,\mu\text{H} & \text{when } P_s = 200\,\text{W}. \end{cases} \quad (40)$$

Solving (40) yields a simple ZVS region in forward operation according to the value of $L_{m1,2}$.

During backward operation, i_{Lm1} discharges C_{S8} and C_{S10} and charges C_{S7} and C_{S9} during the first-half switching period. i_{Lm1} must fully discharge C_{S8} and C_{S10} to achieve ZVS. Then, the ZVS condition in the backward operation becomes

$$(0.5nV_p + \Delta V_{Cr} - V_s)(C_{S7} + C_{S8} + C_{S9} + C_{S10}) < \left| \int_0^{t_{df}} n \cdot i_{Lm1}(\tau) d\tau \right| = I_{Lm1} t_{db}. \quad (41)$$

Substituting $I_{Lm1} = \frac{nV_p(D_b + D_{bz})T_s}{4L_{m1}}$ into (41), we have

$$L_{m1} < \frac{nV_p(D_b + D_{bz}) T_s t_{db}}{4(0.5nV_p + \Delta V_{Cr} - V_s)(C_{S7} + C_{S8} + C_{S9} + C_{S10})} \simeq \begin{cases} 1,500\,\mu\text{H} & \text{when } P_s = 1\,\text{kW} \\ 2,600\,\mu\text{H} & \text{when } P_s = 200\,\text{W}. \end{cases} \quad (42)$$

Here, the falling duty-ratio D_{bz} is identified as

$$D_{bz} = \frac{1}{\omega_r T_s} \cos^{-1} \left[\frac{1}{r_3} (V_s - \Delta V_{Cr} - 0.5nV_p) \right] = \frac{1}{\omega_r T_s} \cos^{-1} \left(\frac{4V_s^2 C_r M_b (1 - M_b) - P_s T_s}{4V_s^2 C_r M_b (1 - M_b) + P_s T_s} \right). \quad (43)$$

By choosing a small magnetizing inductance in (40), it is possible to achieve full-range ZVS during forward operation. By substituting (26) and (43) into (42), we demonstrate the ZVS region during backward operation using the values of $L_{m1,2}$, $I_{Lm1,2}$, P_s, and M_b (see Fig. 7). While a small $L_{m1,2}$ can increase the ZVS region of the proposed converter, it may also generate high peaks in $i_{Lm1,2}$ and disrupt ZCS. In addition, a large $L_{m1,2}$ inevitably generates a large leakage inductance. Thus, an appropriate value of $L_{m1,2}$ must be selected to achieve both an acceptable ZVS region and a low peak in $i_{Lm1,2}$. The resulting $L_{m1,2}$ is 700 μH.

D. Resonant Inductance and Resonant Capacitance

In order for the converter to function properly, C_r needs to satisfy

$$\Delta V_{Cr} \le V_s. \quad (44)$$

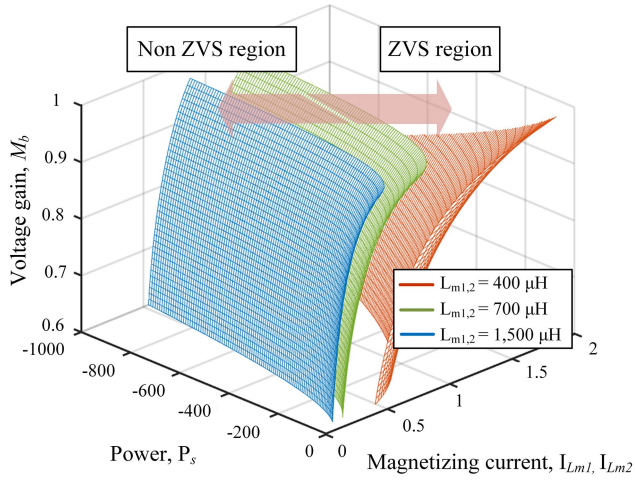

Fig. 7. ZVS region of the proposed converter with respect to I_{Lm1}, I_{Lm2}, P_s, and M_b at backward operation.

Substituting (14) into (44), we then have

$$C_r \ge \frac{P_s T_s}{2nV_p V_s} = \frac{1,000 \times \frac{1}{100,000}}{2 \times 4.0 \times 200 \times 400} = 15.65\ \text{nF}. \quad (45)$$

When P_s is high, the voltage fluctuation in the capacitor becomes high, and so the capacitor must have a sufficiently high value to satisfy (45). Using $\omega_r = 1/\sqrt{L_r C_r}$ and (45) yields

$$L_r \le \frac{2nV_p V_s}{\omega_r^2 P_s T_s} = \frac{2 \times 4.0 \times 200 \times 400}{(109\,827 \times 2\pi)^2 \times 1,000 \times \frac{1}{100\,000}} = 134.4\ \mu\text{H}. \quad (46)$$

To increase the rated power of the converter, L_r must be reduced. However, it is also important to keep the current stress on the active devices to a minimum. To achieve this, L_r should be as large as possible, but not so large as to violate (46). If f_r is set higher than f_s, then the converter can meet ZCS condition during forward operation

$$D_f + D_{fz} < 0.5 \quad (47)$$

where the falling duty-ratio D_{fz} is identified as

$$D_{fz} = \frac{1}{\omega_r T_s} \cos^{-1} \left[\frac{1}{r_2} (V_s - \Delta V_{Cr} - 0.5nV_p) \right] = \frac{1}{\omega_r T_s} \cos^{-1} \left(\frac{n^2 V_p^2 C_r (M_f - 1) - P_s T_s}{n^2 V_p^2 C_r (M_f - 1) + P_s T_s} \right). \quad (48)$$

Rearranging (47) with regard to L_r yields

$$L_r < \frac{1}{C_r} \frac{0.5 T_s}{\cos^{-1} \left(\frac{V_s P_s T_s M_f (2 - M_f) + 4V_s^3 C_r}{4V_s^3 C_r + V_s P_s M_f^2} \right) + \cos^{-1} \left(\frac{n^2 V_p^2 C_r (M_f - 1) - P_s T_s}{n^2 V_p^2 C_r (M_f - 1) + P_s T_s} \right)}. \quad (49)$$

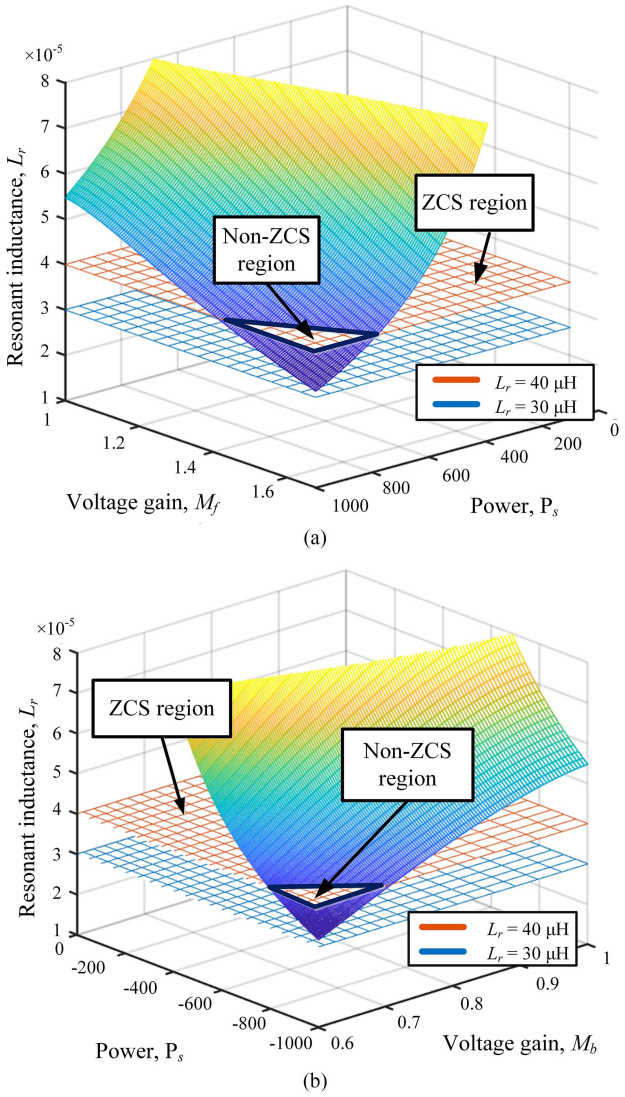

Fig. 8. ZCS region of the proposed converter according to the different values of L_r. The colored curved surfaces depict the upper boundary value of L_r to satisfy the ZCS condition for a given voltage conversion ratio and power. The flat surfaces display the values of L_r for the comparison. (a) Forward operation. (b) Backward operation.

In the backward operation, the ZCS condition is

$$D_b + D_{bz} < 0.5. \tag{50}$$

Rearranging (50) with regard to L_r yields

$$L_r < \frac{1}{C_r} \frac{0.5T_s}{\cos^{-1}\left(\frac{V_s P_s T_s(2M_b-1)+4V_s^3 C_r(M_b-1)}{4V_s^3 C_r(M_b-1)-V_s P_s T_s}\right) + \cos^{-1}\left(\frac{4V_s^2 C_r M_b(1-M_b)-P_s T_s}{4V_s^2 C_r M_b(1-M_b)+P_s T_s}\right)}. \tag{51}$$

To achieve ZCS in both power flow directions, L_r must meet the conditions given in (49) and (51). Once appropriate values for L_r and C_r have been chosen, the ZCS condition will always be satisfied for both forward operation [see Fig. 8(a)] and backward operation [see Fig. 8(b)]. The resulting L_r is 30 μH.

TABLE II
PARAMETERS AND COMPONENTS OF THE PROTOTYPE

Parameters	Symbols	Value
Primary source voltage	V_p	150 – 200 V
Secondary source voltage	V_s	400 V
Output power	P_s	1 kW
Switching frequency	f_s	100 kHz
Resonant frequency	f_r	109.8 kHz
Turns ratio	N_p:N_{s1}:N_{s2}	18:36:36
Magnetizing inductance	L_{m1},L_{m2}	700 μH
Resonant inductance	L_r	30 μH
Resonant capacitance	C_r	70 nF
Primary capacitance	C_p	20 μF
Secondary capacitance	C_s	20 μF
Dead time	t_{df},t_{db}	150 ns
Components	**Symbol**	**Part number**
Primary side switches	$S_1 - S_4$	IPP200N25N3
Secondary-side switches	S_5, S_6	UJ3C065030K3S
Secondary-side switches	$S_7 - S_{10}$	IPP60R060C7
Transformer core	T	PQ5050 x 2
Resonant inductor core	L_r	PQ3535

V. EXPERIMENTAL RESULTS

To demonstrate the performance of the proposed converter, we carried out experiments using a 1-kW prototype that we built in-house. The primary voltage source ranged from 150 to 200 V, and the secondary voltage source was fixed at 400 V, with a rated secondary power of 1-kW. We included the general circuit component values and specific components used in the experiment (Tables II and III). SiC MOSFETs experience much smaller switching losses at turn-ON and turn-OFF instants than Si MOSFETs. In the proposed converter, only two switches are turned OFF with hard switching in both power flow directions thanks to the switching modulation. Therefore, we used SiC MOSFETs (Part number: UJ3C065030K3S) at those two switches. We have used Si MOSFETs (Part number: IPP200N25N3) for the primary-side switches; we have also used Si MOSFETs (Part number: IPP60R060C7) for the secondary-side switches at the middle leg and right leg. TMS320F28377D digital signal processor is used to execute the proportional–integral current control algorithm. When operating in the forward operation, the converter acts as a PWM resonant boost converter. After turning on S_1 and S_4, the current in the resonant inductor rises rapidly [see Fig. 9(a)]. When S_6 is turned OFF, i_{Lr} drops sinusoidally to zero. During the dead-time, the magnetizing inductor current discharges C_{S1}, which is then switched ON with ZVS at full load [see Fig. 9(b)]. Since i_{S1} has the same waveform as that of i_{S4}, S_4 is turned ON with ZVS. S_5 and S_6 are turned ON with ZVS [see Fig. 9(c)]. Full-load current flows through S_6. Half of the current flows through S_7 and S_9 [see Fig. 9(d)]. On the other hand, when operating in the backward operation, the converter operates as a PWM resonant buck converter, and the current i_{Lr} begins to flow through L_r in a sinusoidal curve as S_7 and S_9 are turned ON [see Fig. 10(a)]. Unlike forward operation, the current i_{Lr} during backward operation includes the current flowing through the magnetizing inductor. Here, the resonant current approaches zero following the sinusoidal waveform. S_5 is turned ON with ZVS [see Fig. 10(b)]. S_7 is turned ON with ZVS and OFF with almost ZCS [see Fig. 10(c)]. Similar to

TABLE III
SPECIFICATION OF THE MAGNETIC COMPONENTS

Parameters of transformer	Value
Core shape	PQ (0T45050UG, Magnetics)
Core material	Ferrite T material
Core size	32.0/51.0/50.0 mm (Length/Width/Height)
Primary winding	18 turns, 340 strands of 38 AWG
Secondary winding	36 turns, 260 strands of 38 AWG
Magnetizing inductance	700 μH
Leakage inductance	2.1 μH
Parameters of external resonant inductor	**Value**
Core shape	PQ (0T43535UG, Magnetics)
Core material	Ferrite T material
Core size	26.6/35.8/32.1 mm (Length/Width/Height)
Winding	15 turns, 200 strands of 38 AWG
Inductance	27.9 μH

forward operation, full-load current flows through S_6. Half of the current flows through S_7 and S_9 [see Fig. 10(d)]. The power conversion efficiency of the proposed converter was assessed using a Yokogawa WT3000 digital power meter [see Fig. 11]. The results indicated that the maximum efficiency was 97.9% in the forward direction and 97.2% in the backward direction. Power loss distributions of the proposed converter are obtained in both power flow directions at full load (see Fig. 12). The switch loss is dominant in total loss in both forward and backward operations. When we operate $S_7, \ldots, S_{10}$ at $V_p = 200$ V and at full-load in the synchronous rectification (SR) mode in forward direction and operate $S_1, \ldots, S_{10}$ in the SR mode in backward direction, theoretical efficiency increases by 0.31% in forward direction and by 0.81% in backward direction.

VI. DISCUSSION

We compared the proposed converter with conventional bidirectional converters in terms of topology, shape of inductor current, efficiency, the number of components, voltage/current stress, etc. (see Table IV, Table V, and Fig. 13). Note that we have conducted the simulation under the same operating condition and obtained the theoretical efficiencies in both forward and backward operations. DAB converter [9] has been widely used for bidirectional power transfer while keeping the benefits of phase-shift full-bridge (PSFB) converter. However, this converter inevitably suffers from the high circulating current problem and high switching loss at the turn-off instant. To reduce the turn-OFF loss, *CLLC* converter [13] has been proposed. It can transfer the power resonantly and so the switching loss at turn-OFF instant is alleviated. However, the battery voltage varies widely, and the switching frequency needs to be high, which increases the switching loss. Resonant DAB converter [19] has been proposed. This converter is controlled based on fixed frequency but with a variable duty-ratio. Therefore, it does not experience high switching loss under the wide battery voltage variation. However, the design of this circuit is complicated and it has a relatively narrow ZVS region. When operating at

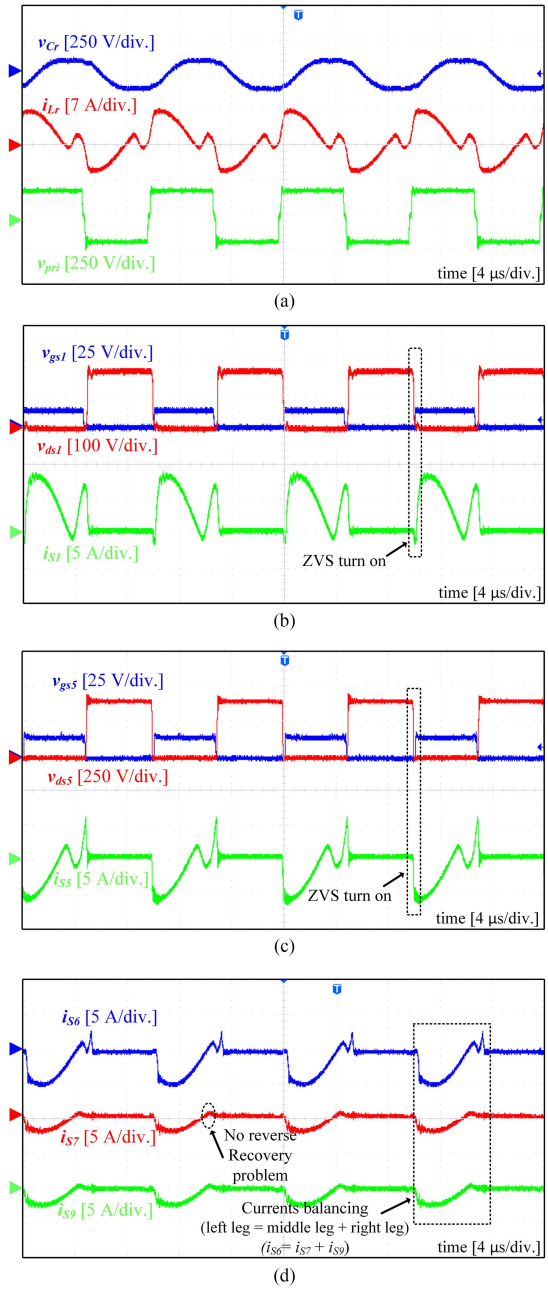

Fig. 9. Experimental waveforms of the proposed converter in forward operation at an intermediate primary voltage $V_p = 175$ V and full load. (a) v_{Cr}, i_{Lr}, and v_{pri}. (b) v_{gs1}, v_{ds1}, and i_{S1}. (c) v_{gs5}, v_{ds5}, and i_{S5}. (d) i_{S6}, i_{S7}, and i_{S9}.

higher power levels, the current flowing through the active power components on the high-voltage side increases. To reduce the current stress, the interleaving structure can be adopted for the converters [9], [19], but this structure significantly increases the number of power components. On the other hand, the proposed converter can be developed with a small number of power components because the left leg is shared in the power processing and only one transformer is used. Phase-shift PWM ensures ZVS turn-ON for both power flow directions. High turn-OFF switching loss occurs only at the secondary-side left leg in both power flow directions; the use of SiC switches only at that leg reduces the

TABLE IV
GENERAL COMPARISON OF CONVENTIONAL BIDIRECTIONAL CONVERTERS AND PROPOSED CONVERTER

References		[9]	[13]	[19]	Proposed
Topology		Dual active bridge (DAB) converter	CLLC converter	Resonant DAB converter	Three-leg active bridge resonant converter
Operation	Forward	Buck–boost	Buck–boost	Buck–boost	Boost
	Backward	Buck–boost	Buck–boost	Buck–boost	Buck
Shape of inductor current	Forward	Linear	Resonant	Resonant	Resonant +resonant
	Backward	Linear	Resonant	Resonant	Resonant +resonant
Rated power		1 kW	1 kW	1 kW	1 kW
Input voltage		150 – 200 V	150 – 200 V	150 – 200 V	150 – 200 V
Output voltage		400 V	400 V	400 V	400 V
Peak efficiency	Forward	95.2%	96.9%	97.8%	97.9%
	Backward	95.7%	96.6%	97.2%	97.2%
Value of components	Inductor	$L_r = 50$ μH	$L_{r1} = 23.3$ μH $L_{r2} = 21.1$ μH	$L_r = 150$ μH	$L_r = 30$ μH
	Capacitor	$C_p, C_s = 20$ μF	$C_p, C_s = 20$ μF $C_{r1} = 110$ nF $C_{r2} = 120$ nF	$C_p, C_s = 20$ μF $C_r = 16.9$ nF	$C_p, C_s = 20$ μF $C_r = 70$ nF
	Turns-ratio	1:2	1:2	1:2	1:4
Switching frequency		100 kHz	100 kHz	100 kHz	100 kHz
Number of components	SiC	4	4	4	2
	Si	4	4	4	6
	Inductors	1	2	1	1
	Transformers	1	1	1	2
	Capacitors	2	4	4	1
Voltage/ current stress in forward operation	Voltage	$S_{1,2,3,4}$ = 200 V $S_{5,6,7,8}$ = 400 V	$S_{1,2,3,4}$ = 200 V $S_{5,6,7,8}$ = 400 V	$S_{1,2,3,4}$ = 200 V $S_{5,6,7,8}$ = 400 V	$S_{1,2,3,4}$ = 200 V $S_{5,6,7,8,9,10}$ = 400 V
	Current	$S_{1,4} \approx 17.8$ A $S_{2,3} \approx 16.8$ A $S_{5,8} \approx 9.9$ A $S_{6,7} \approx 9.9$ A	$S_{1,2,3,4} \approx 8.1$ A $S_{5,6,} \approx 4.0$ A $S_{7,8} \approx 4.1$ A	$S_{1,2,3,4} \approx 7.9$ A $S_{5,7} \approx 4.4$ A $S_{6,8} \approx 4.5$ A	$S_{1,2,3,4} \approx 8.1$ A $S_{5,6} \approx 4.9$ A $S_{7,8,9,10} \approx 2.4$ A
Voltage/ current stress in backward operation	Voltage	$S_{1,2,3,4}$ = 200 V $S_{5,6,7,8}$ = 400 V	$S_{1,2,3,4}$ = 200 V $S_{5,6,7,8}$ = 400 V	$S_{1,2,3,4}$ = 200 V $S_{5,6,7,8}$ = 400 V	$S_{1,2,3,4}$ = 200 V $S_{5,6,7,8,9,10}$ = 400 V
	Current	$S_{1,4} \approx 15.4$ A $S_{2,3} \approx 14.7$ A $S_{5,6} \approx 8.3$ A $S_{7,8} \approx 8.1$ A	$S_{1,2,3,4} \approx 7.1$ A $S_{5,6} \approx 4.2$ A $S_{7,8} \approx 4.7$ A	$S_{1,2,3,4} \approx 7.2$ A $S_{5,7} \approx 4.7$ A $S_{6,8} \approx 4.1$ A	$S_{1,2,3,4} \approx 9.7$ A $S_{5,6} \approx 5.7$ A $S_{7,8,9,10} \approx 2.8$ A

TABLE V
COST COMPARISON OF CONVENTIONAL BIDIRECTIONAL CONVERTERS AND PROPOSED CONVERTER

Component	Part number	Rated value	Unit cost ($)	[9]	[13]	[19]	Proposed
Switches	UJ3C065030K3S	650 V	19.4	4	4	4	2
	IPP200N25N3	250 V	7.1	4	4	4	4
	IPP60R060C7 (IKP40N65H5)	650 V (650 V)	5.5 (3.3)	-	-	-	4
Magnetics	PQ5050	-	12.3	1	1	1	2
	PQ3535	-	9.6	1	2	1	1
Capacitor	-	450 V, 20 μF	7.7	2	2	2	2
	-	400 V, 16.7 nF	1.4	-	-	2	-
	-	400 V, 70 nF	1.5	-	-	-	1
	-	400 V, 110 nF	1.7	-	1	-	-
	-	400 V, 120 nF	1.7	-	1	-	-
Total cost ($)				143.3	156.3	146.1	140.3 (131.5)

*The cost was sourced from www.mouser.com on Feb. 28, 2024.

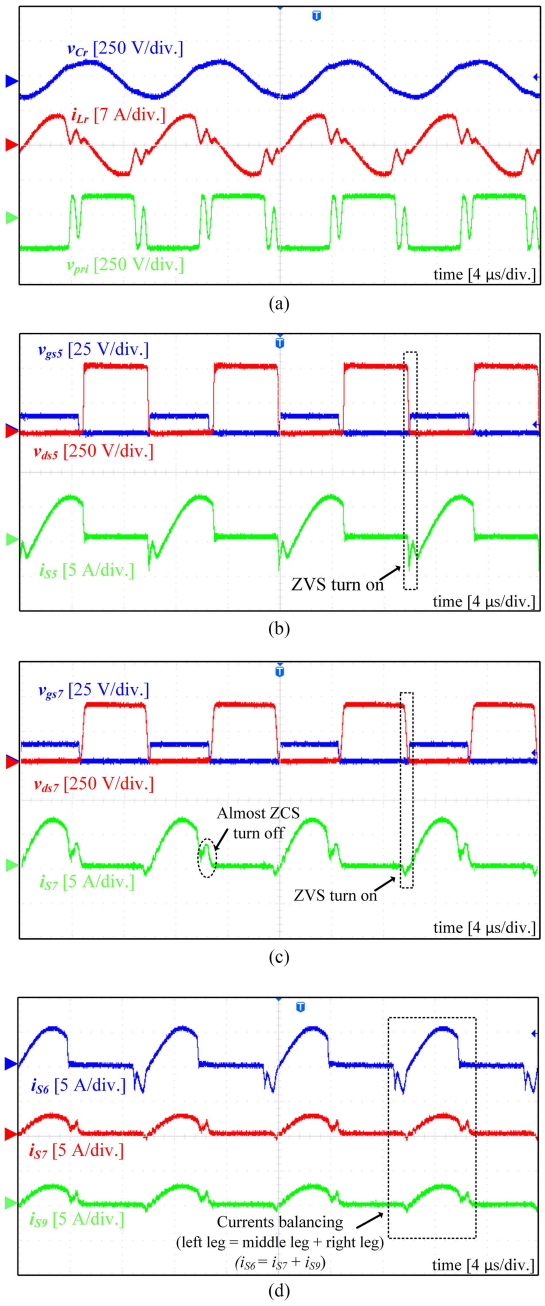

Fig. 10. Experimental waveforms of the proposed converter in backward operation at an intermediate primary voltage $V_p = 175$ V and full load. (a) v_{Cr}, i_{Lr}, and v_{pri}. (b) v_{gs5}, v_{ds5}, and i_{S5}. (c) v_{gs7}, v_{ds7}, and i_{S7}. (d) i_{S6}, i_{S7}, and i_{S9}.

development cost (see Table V). Also, the use of Si insulated gate bipolar transistor (IGBT) (Part number: IKP40N65H5) instead of Si MOSFET on the secondary side can lower the development cost further.

The center-tapped transformer in the proposed converter can be implemented in three different ways. When the primary-side windings are connected in series and each secondary-side winding has wound in the same direction [see Fig. 14(a)], two legs connected to the upper secondary-side transformer have different equivalent circuits with two legs connected to the

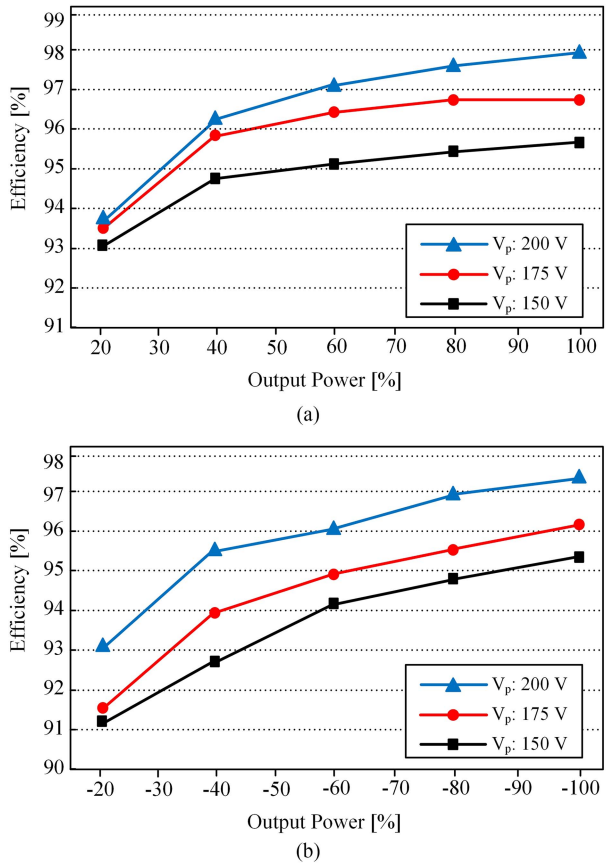

Fig. 11. Experimental efficiency curves according to the different output powers and the primary source voltages. (a) Forward operation. (b) Backward operation.

lower secondary-side transformer. Therefore, the currents flowing through the upper secondary-side transformer and the lower secondary-side transformer are unbalanced. When the primary-side windings are connected in parallel and each secondary-side winding has wound in the opposite direction [see Fig. 14(b)], the secondary-side currents are balanced under the same values of secondary-side leakage inductances of the center-tapped transformer. However, the secondary-side currents are unbalanced under the different values of secondary-side leakage inductances of the center-tapped transformer due to the different impedances of the equivalent circuits. In contrast, when the primary-side windings are connected in series and each secondary-side winding has wound in the opposite direction [see Fig. 14(c)], secondary-side currents are mostly balanced under the different values of secondary-side leakage inductances of the center-tapped transformer.

Remark 1: If we keep charging the battery, it can operate at the nominal voltage. However, if we bring the battery outside and use it for a long time without charging, the battery can be depleted and its voltage level becomes low. In this manuscript, we tried to verify the feasibility of the proposed concept. Thus, the voltage level of a fully charged battery is set to be 200 V and the voltage level of the depleted battery is set to be 150 V. Its

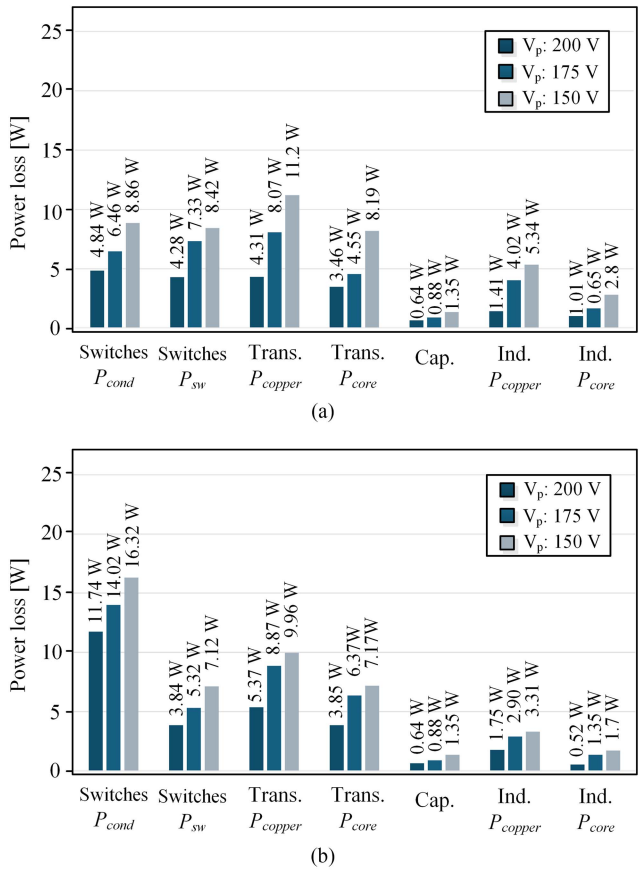

Fig. 12. Theoretical power loss distribution of the proposed converter. (a) Forward operation. (b) Backward operation. Trans., Cap., and Ind. stand for transformer, capacitor, and inductor.

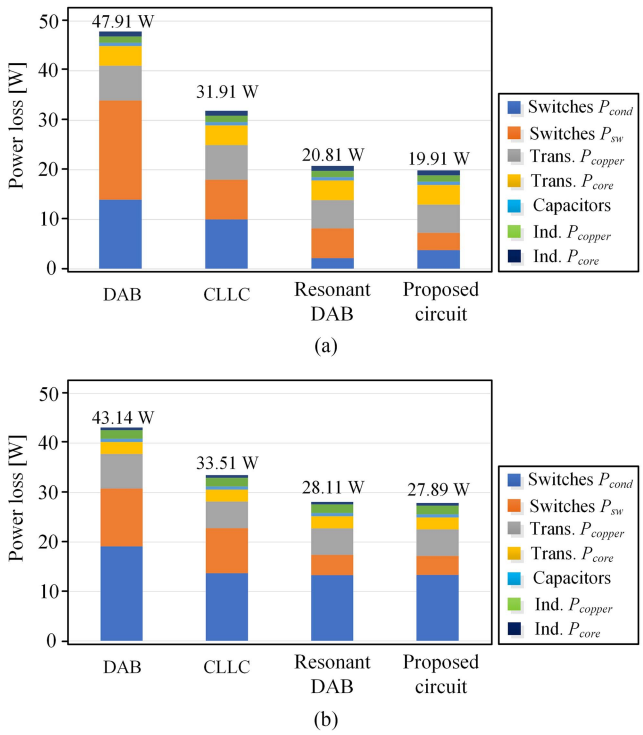

Fig. 13. Theoretical power loss distribution of conventional bidirectional converters and proposed converter. (a) Forward operation. (b) Backward operation.

ratio is 1:1.34 which is close to 1:1.4. At the commercialization stage, the battery voltage range needs to be adjusted further.

Remark 2: The LLC converter is the unidirectional converter and uses pulse frequency modulation. It operates in step-down mode when the switching frequency is set to be higher than the resonant frequency, but operates in step-up mode when the switching frequency is set to be lower than the resonant frequency. The proposed converter is a bidirectional converter and utilizes PWM. This converter operates in step-up mode when it transfers the power in the forward direction and it uses the secondary-side switching, but it operates in step-down mode when it transfers the power in the backward direction and it uses the secondary-side switching. In this case, if we set the switching frequency higher than the resonant frequency, the ZCS region decreases. To ensure the ZCS region under the wide voltage gain variation, we have set the switching frequency lower than the resonant frequency.

Remark 3: When the proposed converter adopts two-legs at the secondary-side, the amount of total power transferred through the secondary side is the same as that for the proposed converter with three-legs at the secondary-side. However, when we use SiC MOSFETs at the left leg and Si MOSFETs at the right leg, the heat that occurs at the right leg is high. Here, SiC MOSFETs are used to reduce the turn-OFF loss that occurred at the switches at the left leg. As we increase the rated power of this converter up to 7.4-kW to be used for the bidirectional on-board battery chargers, each of the primary-side switches experiences the switch loss of 11 W; each of the secondary-side switches at the left leg experiences the switch loss of 17 W; each of the secondary-side switches at the right leg experiences the switch loss of 24 W. Then, the water cooling method needs to be used instead of the air cooling method to dissipate the heat that occurs at the switches on the right leg; this water cooling system increases the development cost and volume of the converter system. To lower the heat that occurs at the switches on the right leg, the proposed three-leg converter can be used. The switches at the middle leg and at the right leg experience switch losses equal to or lower than 17 W, so the air cooling method can be used to dissipate the heat for all the switches; this trait can reduce the development cost and volume of the converter system.

VII. Conclusion

This article introduces a bidirectional resonant converter that utilizes a three-leg active bridge and hybrid Si/SiC switches. The circuit includes a full bridge and a three-leg active bridge where the left leg of the three-leg active bridge is shared in power processing. Compared with the use of two conventional DAB converters, it can save six active power components and an extra transformer. The phase-shift modulation has been used during forward and backward operations, which enables ZVS turn-ON for all the switches. The use of only two SiC MOSFETs reduces the conduction and turn-OFF losses in both power flow directions, thereby decreasing the development cost of the circuit. The symmetric secondary-side winding configuration of the transformer and the corresponding secondary-side switching modulation balance the currents flowing through the secondary-side middle

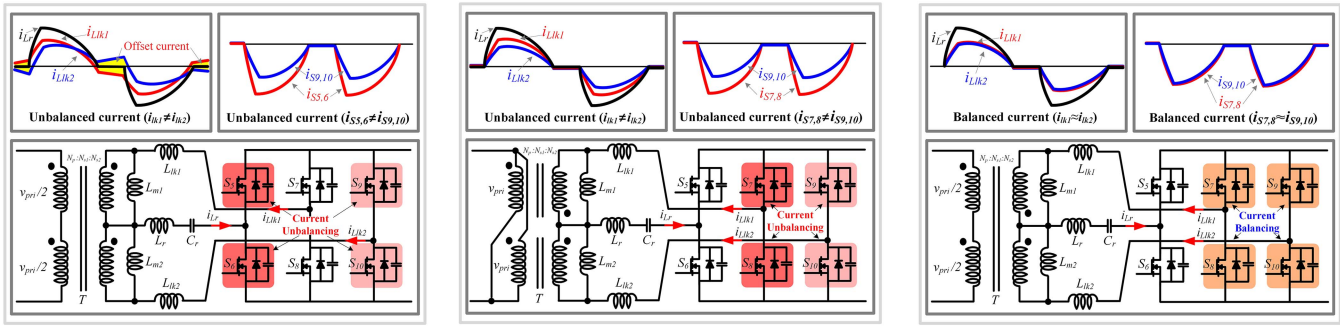

(a) (b) (c)

Fig. 14. Currents flowing through the secondary side of the circuit according to the different connections of the windings of the transformer under 20% parameters mismatch; L_{m1}=700 μH, L_{m2}=560 μH, L_{lk1}=2.1 μH, and L_{lk2}=2.52 μH; strong red shaded area indicates a high switch loss, light red shaded area indicates a low conduction loss, and light brown area indicates a middle conduction loss. (a) Primary-side windings are connected in series and each secondary-side winding has wound in the same direction. (b) Primary-side windings are connected in parallel and each secondary-side winding has wound in the opposite direction. (c) Primary-side windings are connected in series and each secondary-side winding has wound in the opposite direction.

leg and right leg. To validate the effectiveness of the proposed converter, we constructed a 1-kW prototype and demonstrated its expected operation.

REFERENCES

[1] IMARC Group, "Battery market: Global industry trends, share, size, growth, opportunity, and forecast 2022–2027," Apr. 2022.

[2] R. Mottet, M. Almanza, L. Pniak, A. Boegli, and Y. Perriard, "Ultra-high-voltage (7-kV) bidirectional flyback converter used to drive capacitive actuators," *IEEE Trans. Ind. Appl.*, vol. 57, no. 5, pp. 5145–5156, Sep./Oct. 2021.

[3] N. T. Milas and E. C. Tatakis, "Fast battery cell voltage equaliser based on the bi-directional flyback converter," *IEEE Trans. Transp. Electrif.*, vol. 9, no. 4, pp. 4922–4940, Dec. 2023.

[4] J. W. Lim, J. Hassan, and M. Kim, "Bidirectional soft switching push–pull resonant converter over wide range of battery voltages," *IEEE Trans. Power Electron.*, vol. 36, no. 11, pp. 12251–12267, Nov. 2021.

[5] M. S. Rana, S. Suresh, and S. K. Mishra, "A voltage-fed soft-switched push–pull topology with phase-shifted power transfer using coupled LC snubber," *IEEE Trans. Power Electron.*, vol. 36, no. 12, pp. 13903–13916, Dec. 2021.

[6] M. Schulz and S. Ditze, "Analysis and experimental verification of an isolated half-bridge bidirectional DC-DC converter," *IEEE Trans. Power Electron.*, vol. 37, no. 5, pp. 5089–5106, May 2022.

[7] H. Fan and H. Li, "High-frequency transformer isolated bidirectional DC–DC converter modules with high efficiency over wide load range for 20 kVA solid-state transformer," *IEEE Trans. Power Electron.*, vol. 26, no. 12, pp. 3599–3608, Dec. 2011.

[8] B. Han, C. Bai, J. S. Lee, and M. Kim, "Repetitive controller of capacitorless current-fed dual-half-bridge converter for grid-connected fuel cell system," *IEEE Trans. Ind. Electron.*, vol. 65, no. 10, pp. 7841–7855, Oct. 2018.

[9] H. Wen, J. Li, H. Shi, Y. Hu, and Y. Yang, "Fault diagnosis and tolerant control of dual-active-bridge converter with triple-phase shift control for bidirectional EV charging systems," *IEEE Trans. Transp. Electrif.*, vol. 7, no. 1, pp. 287–303, Mar. 2021.

[10] E. L. Carvalho, C. A. Felipe, L. V. Bellinaso, C. M. de Oliveira Stein, R. Cardoso, and L. Michels, "Asymmetrical-PWM DAB converter with extended ZVS/ZCS range and reduced circulating current for ESS applications," *IEEE Trans. Power Electron.*, vol. 36, no. 11, pp. 12990–13001, Nov. 2021.

[11] C. Song, A. Sangwongwanich, Y. Yang, and F. Blaabjerg, "A model-free capacitor voltage balancing method for multilevel DAB converters," *IEEE Trans. Power Electron.*, vol. 38, no. 1, pp. 79–84, Jan. 2023.

[12] C. Liu, S. Liu, Y. Chen, X. Zou, and Y. Kang, "Hybrid-type DAB converter with DC blocking capacitor for ultra-wide input-voltage range," *IEEE Trans. Power Electron.*, vol. 38, no. 6, pp. 6784–6789, Jun. 2023.

[13] H. Chen, K. Sun, L. Lu, S. Wang, and M. Ouyang, "A constant current control method with improved dynamic performance for CLLC converters," *IEEE Trans. Power Electron.*, vol. 37, no. 2, pp. 1509–1523, Feb. 2022.

[14] H. Chen, K. Sun, H. Shi, J. Ha., and S. Lee, "A battery charging method with natural synchronous rectification features for full-bridge CLLC converters," *IEEE Trans. Power Electron.*, vol. 37, no. 2, pp. 2139–2151, Feb. 2022.

[15] Y. Xu, X. Dai, Z. Zhang, Z. Kang, and T. Jin, "A novel phase-shift pulsewidth modulation method for light-load bidirectional resonant converter," *IEEE Trans. Power Electron.*, vol. 38, no. 3, pp. 3257–3267, Mar. 2023.

[16] J. Min and M. Ordonez, "Bidirectional resonant CLLC charger for wide battery voltage range: Asymmetric parameters methodology," *IEEE Trans. Power Electron.*, vol. 36, no. 6, pp. 6662–6673, Jun. 2021.

[17] S. A. Ansari, J. N. Davidson, and M. P. Foster, "Fully-integrated transformer with asymmetric primary and secondary leakage inductances for a bidirectional resonant converter," *IEEE Trans. Ind. Appl.*, vol. 59, no. 3, pp. 3674–3685, May/Jun. 2023.

[18] F. M. Ibanez, J. M. Echeverria, J. Vadillo, and L. Fontan, "A step-up bidirectional series resonant DC/DC converter using a continuous current mode," *IEEE Trans. Power Electron.*, vol. 30, no. 3, pp. 1393–1402, Mar. 2015.

[19] H. P. Park, M. Kim, and J. H. Jung, "Investigation of zero voltage switching capability for bidirectional series resonant converter using phase-shift modulation," *IEEE Trans. Power Electron.*, vol. 34, no. 9, pp. 8842–8858, Sep. 2019.

[20] M. Yaqoob, K. H. Loo, and Y. M. Lai, "Fully soft-switched dual-active-bridge series-resonant converter with switched-impedance-based power control," *IEEE Trans. Power Electron.*, vol. 33, no. 11, pp. 9267–9281, Nov. 2018.

[21] S. Hu, X. Li, and A. K. Bhat, "Operation of a bidirectional series-resonant converter with minimized tank current and wide ZVS range," *IEEE Trans. Power Electron.*, vol. 34, no. 1, pp. 904–915, Jan. 2019.

[22] C. Yu et al., "High efficiency bidirectional dual active bridge (DAB) converter adopting boost-up function for increasing output power," *IEEE Trans. Power Electron.*, vol. 37, no. 12, pp. 14678–14691, Dec. 2022.

[23] C. Bai and M. Kim, "Bidirectional resonant converter with minimized switching loss over wide operating voltage range," *IEEE Trans. Emerg. Sel. Topics Power Electron.*, vol. 10, no. 3, Jun. 2022.

[24] X. Zhu, K. Liu, B. Zhang, and K. Jin, "Multiphase BHB-CLL resonant converter based on secondary side VDR with automatic current sharing characteristic," *IEEE Trans. Ind. Electron.*, vol. 71, no. 2, pp. 1443–1455, Feb. 2024.

[25] D. Yang, B. Duan, W. Ding, C. Zhang, J. Song, and H. Bai, "Turn-off delay-controlled bidirectional DC–DC resonant converter with wide gain range and high efficiency," *IEEE Trans. Transp. Electrif.*, vol. 6, no. 1, pp. 118–130, Mar. 2020.

[26] M. Nitzsche, C. Cheshire, M. Fischer, J. Ruthardt, and J. Roth-Stielow, "Comprehensive comparison of a SiC MOSFET and Si IGBT based inverter," in *Proc. PCIM Europe Int. Exhib. Conf. Power Electron. Intell. Motion, Renewable Energy Energy Manage.*, May 2019, pp. 1828–1834.

[27] R. W. Erickson and D. Maksimovic, *Fundamentals of Power Electronics*. Berlin, Germany: Springer, 2007.

[28] "Catalog on ferrite cores," *Magnetics*, 2021.

Cheol-Hwan Kim (Student Member, IEEE) was born in Chungju, South Korea, in 1997. He received the B.S. and M.S. degrees in electronics and electrical engineering from Dongguk University, Seoul, South Korea, in 2022 and 2024, respectively.

His research interests include bidirectional power conversion circuits for battery systems and resonant converters for electric vehicles and energy storage systems.

Changkyu Bai (Member, IEEE) was born in Seoul, South Korea, in 1993. He received the B.S. degree in electrical engineering and the Ph.D. degree in convergence IT engineering from the Pohang University of Science and Technology, Pohang, South Korea, in 2016 and 2021, respectively.

He is currently a Senior Researcher with Mando Corporation Global Research and Development Center, Seongnam, South Korea. His research interests include bidirectional power conversion circuit for battery systems, highly efficient power conversion circuit design for renewable energy systems, and power supply design for wide bandgap devices.

Sang-Won Lee (Member, IEEE) received the B.S. degree in electrical engineering from Kyungpook National University, Daegu, South Korea, in 2014, and the M.S. and Ph.D. degrees in electrical and electronics engineering from the Pohang University of Science and Technology, Pohang, South Korea, in 2016 and 2020, respectively.

He is currently an Assistant Professor with the Department of Electrical, Electronics and Control Engineering, Kongju National University, Cheonan, South Korea.

Eun-Ha Park was born in Bucheon, Korea, in 2000. She received the B.S. degree in electronics and electrical engineering in 2023 from Dongguk University, Seoul, South Korea, where she is currently working toward the M.S. degree in electronics and electrical engineering from Dongguk University, Seoul, South Korea.

Her research interests include power conversion systems and control, grid-connected inverters, and renewable energy systems and electric vehicles.

Minsung Kim (Senior Member, IEEE) was born in Ulsan, South Korea, in 1986. He received the B.S. and Ph.D. degrees in electrical engineering from the Pohang University of Science and Technology (POSTECH), Pohang, South Korea, in 2008 and 2013, respectively.

Since 2013, he has been with Department of Creative IT Engineering and Future IT Research Laboratory, POSTECH, where he was a Research Assistant Professor. In 2016, he has worked as Research Scholar in Future Energy Electronics Center with Virginia Tech, Blacksburg, VA, USA. In 2017 and 2018, he has also served as Academic Visitor in Control and Power System Group at Imperial College London, London, U.K. Since 2018, he has been with the Division of Electronics and Electrical Engineering, Dongguk University, Seoul, South Korea, where he is currently an Associate Professor. His current research interests include highly efficient power conversion circuit design, intelligent controller design for industrial electronics, and renewable energy and energy storage systems.